This is a preprint, the final version is subject to change, of the American Mineralogist (MSA)
Cite as Authors (Year) Title. American Mineralogist, in press.
(DOI will not work until issue is live.) DOI: http://dx.doi.org/10.2138/am-2015-5237

Revision 1

Synthesis of Large and Homogeneous Single Crystals of Water-Bearing Minerals by Slow Cooling at Deep-Mantle Pressures

Takuo Okuchi[1*], Narangoo Purevjav[1], Naotaka Tomioka[1], Jung-Fu Lin[2], Takahiro Kuribayashi[3], Louise Schoneveld[4]†, Huijeong Hwang[5], Naoya Sakamoto[6], Noriyuki Kawasaki[7], and Hisayoshi Yurimoto[7]**

[1] Institute for Study of the Earth's Interior, Okayama University, Misasa, Tottori 682-0193, Japan
[2] Department of Geological Sciences, Jackson School of Geosciences, University of Texas at Austin, Austin, TX 78712-0254, USA
[3] Department of Earth Science, Graduate School of Science, Tohoku University, Sendai 980-8578, Japan
[4] School of Earth and Environmental Sciences, James Cook University, Townsville, QLD 4811, Australia
[5] College of Science, Yonsei University, Seoul 120-749, South Korea
[6] Creative Research Institution, Hokkaido University, Sapporo, 0010021, Japan
[7] Department of Natural History Sciences, Hokkaido University, Sapporo, 0600810, Japan

**Present Address: Kochi Institute for Core Sample Research, Japan Agency for Marine-Earth Science and Technology, Nankoku, 783-8502 Kouchi, Japan
†Present Address: Research School of Earth Science, Australian National University, Canberra, ACT, 2602 Australia

*Corresponding author. Email: okuchi@misasa.okayama-u.ac.jp

Abstract

The presence of water in the Earth's deep mantle is an issue of increasing interest in the field of high-pressure mineralogy. An important task for further advancing research in the field is to create homogeneous single crystals of candidate deep-mantle

water-bearing minerals of 1 mm or larger in size, which is required for applying them for the Time-of-Flight (TOF) single-crystal Laue diffraction method with a third-generation neutron instrument. In this study, we perform several experiments to demonstrate an improved methodology for growing hydrous crystals of such large sizes at relevant transition zone and lower-mantle conditions via very slow cooling over a maximum period of 1 day. Successfully synthesized crystals using this methodology include dense hydrous magnesium silicate (DHMS) phase E, hydrous wadsleyite, hydrous ringwoodite, and bridgmanite (silicate perovskite). It is also demonstrated that these hydrous crystals can be grown from deuterium enriched starting materials in addition to from those having natural hydrogen isotope ratio.

Magnitudes of chemical and crystallographic heterogeneities of the product crystals were characterized by comprehensive analysis of X-ray precession photography, single-crystal X-ray diffraction (SCXRD), field-emission scanning electron microscope (FE–SEM), electron probe microanalyser (EPMA), secondary ion mass spectroscopy (SIMS), powder X-ray diffraction (PXRD), and TOF neutron powder diffraction (TOF–NPD). The product crystals were confirmed to be inclusion free and crystallographically homogeneous. Compositional and isotopic homogeneities of major elements and hydrogen isotope abundances were better than 1 % and 3 %, respectively,

among intracrystals and intercrystals within each recovered sample capsule. Phase E crystals up to 600 μm in the largest dimension were grown at a constant temperature of 1100 °C kept for 3 h. Using a lattice parameter-to-temperature relation of phase E, thermal gradient in the sample capsules for its synthesis has been evaluated to be 20 °C/mm. Hydrous wadsleyite crystals with up to 1100 μm in the largest dimension were grown at 1390 °C with a temperature reduction of 70 °C during heating for 10 h. Hydrous ringwoodite crystals with up to 1000 μm in the largest dimension were grown at around 1400 °C with a temperature reduction of 110 °C during heating for 12 h. Bridgmanite crystals with up to 600 μm in the largest dimension were grown at 1700 °C with a temperature reduction of 30 °C during heating for 12 h. A TOF single-crystal diffraction instrument has been successfully used for analyzing one of the hydrous wadsleyite crystals, which demonstrated that appropriate single crystals for their expected usage are created using the method proposed in the present study.

Keywords: Hydrous minerals, Single crystal growth, Phase E, Wadsleyite, Ringwoodite, Bridgmanite, Slow-cooling method

Introduction

Water, an essential component of the Earth, exists in surface oceans and in deep-mantle hydrous minerals (Inoue et al. 1995; Kanzaki 1991; Kohlstedt et al. 1996; Litasov et al. 2003; Pearson et al. 2014). Recent research has suggested that part of the oceanic water is being transported into the deep mantle through the subducting lithosphere to affect the Earth's global dynamic and chemical cycles (Bercovici and Karato 2003; Ohtani et al. 2004; Schmandt et al. 2014). In the Earth's early evolution, primordial water was partitioned among deep-mantle minerals, silicate melt, and metallic Fe alloy (Bolfan-Casanova et al. 2000; Inoue et al. 2010; Okuchi 1997; Shibazaki et al. 2009). Both transported water and that partitioned into the deep-mantle minerals affect the relevant mantle redox state (McCammon et al. 2004; Mrosko et al. 2013; Smyth et al. 2014). The existence of such water has been partly confirmed by a recent discovery of natural hydrous ringwoodite with 1.4 wt% water occurring as an inclusion in a diamond specimen (Pearson et al. 2014). This discovery indicates that at least some areas of the transition zone are enriched with a significant amount of water.

Hydrous deep-mantle minerals contain water as hydroxyl groups (Keppler and Smyth 2006). Numerous experimental results indicate that the physical properties of the host minerals change dramatically with an increase in hydroxyl concentration. These

properties include melting behavior (Inoue 1994; Schmandt et al. 2014), phase relations (Ghosh et al. 2013; Ohtani et al. 2000), transformation kinetics (Kubo et al. 1998), rheology (Chen et al. 1998), and sound velocities (Inoue et al. 1998; Mao et al. 2011, 2012). An important task for further advancing the research on the effects of these hydroxyls is to create well-characterized, homogeneous, hydrous crystals of at least 1 mm in size. This is minimum size requirement to use the Time-of-Flight (TOF) single-crystal Laue diffraction method with a third-generation neutron instrument such as TOPAZ at the Spallation Neutron Source (SNS) (Schultz et al. 2014). Using this state-of-the-art instrument will enable for the first time accurate determination of the position and occupancy of normal hydrogen atoms in the crystal structures of deep-mantle minerals, and therefore direct observation of chemical bonding distance and charge substitution mechanism of the hydrogen. Moreover, accurate atomic displacement parameters of the hydrogen can be measured with this instrument for crystals 1 mm or larger (Jorgensen et al., 2014). These parameters provide invaluable information about chemical bonding strength and directionality of the hydrogen, which is essential to understand and forecast how hydroxyls control the physical properties of minerals.

105 In the present study, we therefore synthesized such crystals of hydrous wadsleyite
106 and hydrous ringwoodite, which are highly expected to occur or have been confirmed
107 within the mantle transition zone. In addition, we synthesized dense hydrous
108 magnesium silicate (DHMS) phase E with a deuterium-enriched composition in crystals
109 up to 600 μm in size, which is a representative hydrous mineral that may occur in
110 hydrated deep-mantle peridotite (Kanzaki et al. 1991; Ohtani et al. 2004). Although the
111 crystal size is smaller than 1 mm, it may be applicable for TOF single-crystal diffraction
112 because deuterium scatters neutrons more coherently and induces much less background
113 than normal hydrogen, in which the required crystal volume is smaller (Wenk 2006).
114 Moreover, the deuterium-enriched crystals will be useful for investigating the hydrogen
115 isotope fractionation phenomena occurring within the deep mantle (Chakoumakos et al.
116 2013; Horita et al. 2010; Okuchi et al. 2014; Yang et al. 2014). In addition to the DHMS
117 Phase E, therefore, ringwoodite crystals were also synthesized in a deuterium-enriched
118 growth environment. Finally, lower-mantle bridgmanite (silicate perovskite) crystals
119 100 μm to 600 μm in size were synthesized in normal water (H_2O)-bearing growth
120 environments. Although we were unable to grow these bridgmanite crystals into
121 suitable sizes for TOF single-crystal diffraction, some proved to be ideal for use in

advanced high-pressure–high-temperature X-ray and laser experiments (e.g., Goncharov et al. submitted).

It is reasonable to expect that crystals grown into larger sizes may become less homogeneous. We therefore consider that it is important to evaluate the chemical and crystallographic heterogeneity of the synthesized crystals. For this purpose, the crystals were comprehensively analyzed using X-ray precession photography, single-crystal X-ray diffraction (SCXRD), field-emission scanning electron microscope (FE–SEM), electron probe microanalyzer (EPMA), secondary ion mass spectroscopy (SIMS), powder X-ray diffraction (PXRD), and TOF neutron powder diffraction (TOF–NPD). In particular, we made a special effort to evaluate the hydrogen and deuterium concentration distributions within each crystal and among the crystals within each capsule of the selected run charges.

Experimental strategy

Previous studies of high-pressure syntheses of deep-mantle crystals have partly addressed the aforementioned research task (Ito and Weidner 1986; Jacobsen et al. 2004; Shatskiy et al. 2007, 2009; Smyth et al. 2003). Of particular interest are crystals of ringwoodite up to 800 μm in size (Jacobsen et al. 2004; Smyth et al. 2003), and those

of wadsleyite and bridgmanite up to 1 mm in size (Shatskiy et al. 2007, 2009). Most of these crystals were grown over a relatively short period within a few hours. For the latter two products, the chemical gradients were intentionally introduced in addition to an existing thermal gradient (≥20 °C/mm) under the extreme pressure–temperature environments of the sample capsules in which the crystals were quickly grown over short periods between 20 min to 3 h, except for one run at 5 h. Although these gradients played very essential roles in the successful synthesis of large and isometric crystals in short periods, they may also induce crystallographic heterogeneities due to fast growth, including lattice defects, crystal inclusions, twinning, and misorientation (Rudolph 2010), which were observed to exist within some of the crystals (Shatskiy et al. 2009). In order to apply the TOF single-crystal diffraction method, samples having these crystallographic heterogeneities are not very appropriate (Wenk, 2006).

In the present study, we used a significantly slower growth rate over a maximum period up to 24 h to produce the sample crystals. In addition, we grew the crystals from a homogeneous silicate melt batch with a volume as large as possible to enable continuous buffering of the crystal's chemical composition. The temperature of the cell slowly decreased during the long heating durations so that the crystals were almost kept in chemical equilibrium with the silicate melt throughout the growth process. This

159 slow-cooling method has been reported as an effective scheme for recovering large and
160 homogeneous crystals of metal oxides from limited sample volumes confined at high
161 pressures up to 11 GPa (Loeffert et al. 2002; Shatskiy et al. 2010; Tamura et al. 1974).
162 In the present study, we extended this method to higher pressures and temperatures of
163 up to 24 GPa and about 1800 °C, respectively, for the crystal growth of deep-mantle
164 hydrous mineral phases.

165

166 **Experimental methods**
167

168 DHMS phase E, pure magnesian hydrous wadsleyite, and pure magnesian and
169 iron-bearing hydrous ringwoodite were synthesized at pressures between 14 GPa and 21
170 GPa and temperatures between 1100 °C and 1400 °C. Bridgmanite with three different
171 compositions was synthesized at 24 GPa and 1650 °C to 1760 °C. Table 1 shows a
172 summary of these experimental conditions yielding relatively large crystal products. We
173 used the scaled-up Kawai-type cell installed at the Institute for Study of the Earth's
174 Interior at Okayama University (Shatskiy et al. 2011). Two different types of cell
175 assembly designs suitable for two different pressure regimes were prepared. Fujilloy
176 F08 tungsten carbide anvils with 8 mm or 6 mm in truncation edge length (TEL) were
177 used to compress these cells, which commonly had $MgO–Cr_2O_3$ pressure media of 14

178 mm in the octahedral edge length (OEL) (Figure 1). Anvils 46 mm in size were used for
179 applied loads of more than 10 MN, and those 32 mm in size were used for loads of less
180 than 10 MN. The efficiency of the pressure generated by using these applied loads was
181 previously calibrated for the combination of 14 mm OEL and 8 mm or 6 mm TEL
182 (Frost et al. 2004; Shatskiy et al. 2009, 2011). Figure 1(a) shows a cross section of the
183 cell coupled with 8 mm TEL, which was used for the phase E, wadsleyite and
184 ringwoodite synthesis. This cell design was established in our previous work for mass
185 production of fully deuterated ringwoodite powder (Purevjav et al. 2014a). In the
186 present study, the same gold capsule of 4 mm in diameter and 5 mm in length in this
187 cell, with ~50 mm^3 in sample volume, was successfully used for the significantly longer
188 heating durations required for single-crystal growth. Figure 1(b) shows the cross section
189 of the other cell coupled with 6 mm TEL, which was used for the bridgmanite synthesis.
190 This capsule was designed and tested to be highly durable at temperatures of at least up
191 to 1800 °C, at which the required long-duration runs were conducted in a stable manner.
192 A platinum capsule of 2 mm in diameter and 4 mm in length, with ~12 mm^3 in sample
193 volume, was successfully used at even higher temperatures than those used in previous
194 bridgmanite growth experiments (Ito and Weidner 1986; Shatskiy et al. 2007). The melt

fraction and the chemical transport efficiency simultaneously increased at the higher temperatures at which we expected more homogeneous crystals to grow.

The starting materials were weighted mixtures of the components suitable for each synthesis (Table 1). Magnesium hydroxide [$Mg(OH)_2$], aluminum oxide [Al_2O_3], iron [Fe], and its oxide [FeO] were prepared from commercial reagents. Part of the iron and its oxide were enriched in ^{57}Fe for the expected applications in Mössbauer spectroscopy and nuclear resonant inelastic X-ray scattering. Silica [SiO_2] was prepared from a high-purity fused silica rod. Magnesium deuteroxide [$Mg(OD)_2$] was prepared by using a hydrothermal reaction of MgO powder and D_2O in an autoclave (Okuchi et al. 2014). For all runs except for EP12-6, the starting materials were the mixtures of these reagents, where H_2O or D_2O wt% was controlled by the weight ratio of $Mg(OH)_2$ or $Mg(OD)_2$ and MgO. Then each mixture was cold-sealed into the capsule to be compressed. For the EP12-6 run for iron-bearing hydrous ringwoodite we adopt a different procedure; powder of ground San Carlos olivine was first filled into the capsule, and liquid H_2O was injected into it. In order to avoid the leakage of H_2O, the capsule was spark-welded, weighed, kept in a vacuum for 1 h, and weighed again to confirm the weight was not changed by evaporation of H_2O.

These capsules were compressed using their relevant cell assembly, anvils, and load (Table 1). After the load reached the desired pressure, the capsule was heated by supplying and controlling the applied electric power. After the desired heating duration passed, the capsule was quenched to room temperature by cutting off the power. We established the power–temperature relations for each cell assembly by conducting several calibration runs in which the temperature of the sample capsule was monitored using a $W_{97}Re_3/W_{75}Re_{25}$ thermocouple inserted into the cell assembly and attached to the capsule. Reproducibility of the calibrated power–temperature relations was within ±5% and ±6% for the 8 mm and 6 mm TEL cell assembly, respectively. Temperatures of the actual synthesis runs were controlled using the supplied power derived from the calibrated power–temperature relations. No correction for the effect of pressure on the thermocouple electromotive force (emf) was applied.

The crystalline portion of the recovered run product from each synthesis experiment was divided into several samples of crystal aggregate. These pieces were first screened using a microfocus X-ray diffractometer (Rigaku RINT RAPID II) to find the mineral phases and to determine whether their Bragg reflections were powder-like rings or spotty. An incident X-ray beam of Cu $K\alpha_{1,2}$ radiation operated at 40 kV and 30 mA was collimated onto a beam size of 100 μm for the analyses. The mineral grains were

oscillated through movements of the omega and phi axes, whereas X-ray diffraction patterns were taken in the reflection mode with an exposure time of 5–20 min. By using this screening process, we quickly evaluated whether the desired crystals with sizes larger than the collimator aperture were recovered. Then, crystallinities of selected samples were further evaluated individually by X-ray precession photography or SCXRD. A precession camera (Rigaku 1533A2) was used for several phase E, hydrogenated magnesian wadsleyite, and hydrogenated magnesian ringwoodite samples using Mo $K\alpha_{1,2}$ radiation operating at 35 kV and 30 mA. Their reciprocal lattice images were taken on an imaging plate with an exposure time of 10 min. SCXRD measurements were conducted by using an automated four-circle X-ray diffractometer (Rigaku AFC-7s) with Mo $K\alpha$ radiation (λ = 0.71073 Å) at the power of 50 kV and 30 mA. This instrument was used to measure crystals of deuterated magnesian ringwoodite and hydrogenated iron-bearing ringwoodite with dimensions of 80 × 50 × 50 μm^3 and 80 × 70 × 50 μm^3. A set of {511} X-ray reflections (24 in total) was used to refine the lattice constants of these ringwoodite crystals.

In addition, we evaluated the chemical heterogeneity of the recovered crystals. The crystals were polished with diamond powder 1 μm in size, coated with carbon, and analyzed using FE–SEM (JEOL JSM-7001F) and EPMA (JEOL JXA-8800). The

248 electron beam was 5–10 μm in diameter, 15 kV in acceleration voltage, and 8–12 nA in
249 current, which were adjusted with consideration to the varying fragility of the sample
250 mineral phases. Analyses of back-scattered electron (BSE) images of the crystals of all
251 synthesized phases by FE–SEM revealed no evidence of chemical zoning. This result
252 was confirmed by major element analyses of these crystals by EPMA, which are
253 detailed subsequently in this paper.

254 Hydrogen and deuterium concentration distributions in the cross sections of phase E,
255 deuterated magnesian ringwoodite, and hydrated iron-bearing ringwoodite crystals were
256 measured by SIMS (CAMECA IMS-6F) at Hokkaido University. A primary $^{133}Cs^{+}$
257 beam operated at 9 nA and 10 kV was focused to a 10 μm spot on the sample, which
258 was coated by gold 50 nm in thickness. Normal incident electron shower was used for
259 electrostatic charge neutralization of sputtering area. The secondary negative ions of
260 hydrogen, deuterium, and ^{30}Si were collected from the spattered area sequentially in an
261 electron multiplier for 10 seconds. Small width of the exit slit was chosen to eliminate
262 the ^{28}SiD interference on the ^{30}Si peak. For quantitative analysis, a natural amphibole
263 containing 1.66 wt% of H_2O was used as a standard material (Miyagi and Yurimoto
264 1995). Both H_2O and D_2O contents in the samples were estimated assuming a linear
265 relationship between their concentrations and the $H/^{30}Si$ or $D/^{30}Si$ ratio (Greenwood et

al. 2011). Other measurement conditions were described elsewhere (Greenwood et al. 2011).

The space group and lattice parameters of the crystals, including those of all phase E, wadsleyite, and ringwoodite run products, were determined via analyses of the PXRD patterns using a few crystalline samples taken from each product (Table 2). All phase E, wadsleyite, and ringwoodite products were successfully indexed with *R*-3*m*, *Imma* and *Fd*-3*m* space groups, respectively, which is consistent with previous structural analysis results. Water concentrations in wadsleyite and ringwoodite were estimated from their refined lattice constants (Jacobsen et al. 2005; Ye et al. 2012). In addition, whole sample products from the two phase E run charges were analyzed by TOF–NPD. The observed reflections in TOF–NPD were successfully indexed with the same *R*-3*m* space group given by the PXRD results, and the linewidth profiles were analyzed in order to estimate the synthesis environments of these phase E products.

For PXRD analysis with the X-ray diffractometer (Rigaku Smartlab), each crystal aggregate sample was ground into a fine powder in an alumina mortar and was measured on an Si low-background plate using the para-focusing method with Cu $K\alpha_1$ radiation operated at 40 kV and 30 mA. The diffraction pattern was obtained by the step scanning method with a 2θ range of 10–140°, step size of 0.005°, and scan speed of

0.1–0.3°/min. The 2θ angles were calibrated by the silicon powder standard (NIST640d) as an external standard, and their lattice constants were refined through least squares fitting of peak positions by using the UnitCell software (Holland and Redfern 1997). For TOF–NPD analysis, each sample was coarsely ground and measured using the TAKUMI Engineering Materials Diffractometer at Materials and Life Science Experimental Facility (MLF), Japan Proton Accelerator Research Complex (J-PARC) (Harjo et al. 2006). For the measurements, the optics of the neutron diffractometer were optimized for analyzing the structure of a hydrous mineral phase with a small sample mass (Okuchi et al. 2014).

Results and Discussion

Figure 2 shows photographs of the recovered single crystals grown by the slow-cooling method. Observations of the samples under an optical microscope confirmed that these crystals had no visible imperfections. In the following sections, the results of microscopic analysis are given and are discussed in a comprehensive manner, demonstrating that these crystals were crystallographically and chemically homogeneous to be suitable for their expected usage. In addition, we show the most

suitable experimental conditions for growing the largest crystals for each synthesized mineral phase.

DHMS phase E crystals

Single crystals of phase E of up to 600 μm in the largest dimension were synthesized in the two relevant experimental runs (Table 1, Figure 2(a)). These crystals were significantly larger than the 100–200 μm size previously reported (Kanzaki 1991; Kleppe et al. 2001; Kudoh et al. 1993). We found that the growth of phase E crystals was remarkably fast even at relatively low temperatures around 1100 °C; therefore, 2–3 h of continuous heating at a constant temperature with a variation of less than ±10 °C was sufficient for recovering these large crystals. This fast crystal growth may be due in part to the very large water concentration (~22 wt%) in the starting material, where below the silicate solidus, a large fraction of aqueous fluid coexisted with the crystals to facilitate the growth (Inoue 1994). It was observed that the capsules were completely filled with phase E crystals that were not sintered to each other, supporting that a large volume fraction of aqueous fluid had coexisted with the crystals.

Figure 3(a) shows a precession photograph of a representative crystal from the PE02 run of 270 × 330 × 530 μm^3. The diffraction spots of the phase E crystal are neither

diffused nor split, which representatively demonstrates absences of stacking disorder and mosaicism in the product crystals. The major element compositions in the cross sections of the other five crystals from the PE02 run showed a slight variation of Mg/Si = 1.83 ±0.03 which may include the effect of thermal gradient within the capsule (Figure 4(a)). The refined lattice constants given in Table 2 were consistent with those reported in previous works determined by precise X-ray diffraction measurements, which expanded between a = 2.9701(1) Å, c = 13.882(1) Å and a = 2.9853(6) Å, c = 13.9482(7) Å (Kleppe et al. 2001; Kudoh et al. 1993). This variation may have been caused by the effects of the synthesis temperature in addition to the Mg/Si molar ratio of the starting materials. Considering the products starting only from Mg/Si = 2, the variation was reduced to between a = 2.9701(1) Å, c = 13.882(1) Å for the sample synthesized at 1000 °C (Kudoh et al. 1993), and a = 2.975(1) Å, c = 13.908(4) Å for the sample synthesized at 1100 °C (Kleppe et al. 2001). Assuming that this variation reflects only the temperature, we estimated the actual synthesis temperature for PE01 at ~1060 °C and PE02 at ~960 °C based on their lattice constants. The consistently lower temperatures by this estimation than the expected values of around 1100 °C may be the result of an isotope effect because the lattice constants can shrink by deuteration, as in the case of brucite having a layered structure similar that of phase E (Horita et al. 2010;

Chakoumakos et al. 2013). We note that the observed occurrences of minor clinoenstatite in PXRD and TOF–NPD patterns of the phase E products in the present study are consistent with a temperature rather close to 1100 °C; otherwise, the clinoenstatite peaks would have disappeared (Inoue 1994). From these observations it is inferred that the lattice parameters are slightly different between deuterated and hydrogenated crystals synthesized at the same temperature, which is desirable to be more quantitatively evaluated by a future study to update the accuracy of temperature scale in the following discussion.

The thermal gradient within each sample capsule was approximated by using the abovementioned lattice-to-temperature relation of the hydrogenated phase E. For this purpose, the full width at half maximum (FWHM) of representative reflections in the whole-capsule TOF–NPD patterns was determined as a function of *d*-spacing (Figure 5). Broadening by $\Delta d/d$ = 0.07% and 0.10%, compared with the original resolution of the diffractometer, was observed for the PE01 and PE02 run charges, which correspond to the averaged thermal inhomogeneity of 40 °C and 60 °C within the whole capsule, respectively. The thermal gradient is thus approximated to be 16–24 °C/mm or 20 ±4 °C/mm for the 2.5 mm length between the center and edge of the capsule shown in Figure 1(a). We note that the observed FWHM values in TOF–NPD patterns were not

increased by particle size and strain effects, because the sample grains are too large to have the size effect and are loosely packed into the sample holder without strain.

We finally discuss hydrogen isotopes of the synthesized phase E crystals. By SIMS analysis of the cross sections of five different crystals from the PE02 run, we found that the isotope abundance of hydrogen in these crystals was uniform at $D/(H + D) = 86 \pm 1$ %, and that total water concentration in these crystals showed little variation (7.9 ±0.6 wt% as H_2O+D_2O; Figure 6(a)). Considering these SIMS results in addition to the major element compositions by EPMA (Figure 4(a)), it was confirmed that these deuterated phase E crystals are suitable for structure refinement or other studies those require chemical and isotopic homogeneity within their entire crystal volumes. The uniform hydrogen isotope abundance of 14 % in all measured crystals indicates that hydrogen was contaminated into the crystals from outside of the capsule such as hydrogen released from an MgO sleeve or $MgO–Cr_2O_3$ pressure medium despite calcination at 1000 °C immediately prior to the cell construction and compression, because isotope abundance of hydrogen was less than 1 % in the deuterated starting material in the capsule (Purevjav et al., 2014a). We are now conducting a structure refinement study of phase E from the TOF–NPD pattern of the PE02 sample having known hydrogen isotope abundance in this study (Tomioka et al. 2014).

374

375 **Hydrous wadsleyite crystals**

376 Single crystals of hydrous magnesian wadsleyite of 400–1100 μm in the largest
377 dimensions were synthesized in the five relevant experimental runs (Table 1). The
378 largest crystal size was 1100 × 800 × 800 μm^3 (Figure 2(b)), which is at least as large as
379 the crystals previously synthesized using a thermal gradient (Shatskiy et al. 2009). From
380 the results of these runs, we found that heating at around 1400 °C along with a reduction
381 of 40 °C to 70 °C was the most effective temperature condition for growing large
382 hydrous wadsleyite crystals, which is 200 °C to 300 °C higher than the wet solidus of
383 the MgO–SiO_2 system (Inoue 1994). The observed melt fraction at this temperature
384 reached about 70% in volume, where efficient buffering of crystal composition is
385 expected to occur.

386 Figure 3(b) shows a precession photograph of a representative wadsleyite crystal
387 from the EP13-2 run of 700 × 500 × 500 μm^3, which demonstrates the high crystallinity
388 of the product crystals. The major element compositions in the cross sections of the
389 other three crystals from the EP13-2 run showed very little variation of Mg/Si = 1.86
390 ±0.01 (Figure 4(a)), indicating that slow cooling of the crystals in large melt fraction is
391 suitable for growing homogeneous hydrous wadsleyite crystals. These analyses also

indicate that the thermal gradient of 20 °C/mm, as estimated in the phase E runs, is too small to induce chemical heterogeneity in these crystals. The averaged H_2O concentration (C_{H2O}) of wadsleyite in each run product including that from EP13-2 was separately estimated from each refined lattice constant (Table 2) using the established relation between the b/a ratio and C_{H2O} (Jacobsen et al. 2005). The estimated C_{H2O} had a variation between 1.6 % for the EP13-2 run quenched at 1250 °C and 1.1% for the HR-18 run quenched at 1320 °C. These results are consistent with the reported systematics of $C_{H2O} = 637e^{-0.0048T}$ (T in °C), which accurately predicted 1.6 wt% at 1250 °C and 1.1 wt% at 1320 °C (Litasov et al. 2011).

A stark contrast of deuterium site positions between hydrous wadsleyite and hydrous ringwoodite has been reported by neutron diffraction of their deuterated powder samples (Purevjav et al. 2014; Sano-Furukawa et al. 2011). Whereas both structures commonly belong to spinel types, it was observed that deuterium in ringwoodite occupies both octahedral and tetrahedral sites, and that in wadsleyite occupies only an octahedral site. In other words, ringwoodite structure is uniquely vulnerable to exchanging silicon cations for hydrogen, which is much more effective for reducing sound velocity and increasing electrical conductivity than exchanging magnesium or iron cations for hydrogen (Mao et al. 2012; Panero et al. 2013). However, like the case

for the current phase E sample, contamination of hydrogen was observed in the Raman spectrum of the wadsleyite powder, which might be the reason for smaller deuterium occupancy around the octahedral site (M3) than the estimation; the observed occupancy was only ~75 % of the calculated value from D_2O concentration of the wadsleyite (Sano-Furukawa et al. 2011).

The problem of hydrogen contamination can be completely eliminated by using the crystals synthesized in the present study. Because single crystal diffraction method is in principle fully tolerable for incoherent scattering induced by hydrogen, crystals involving natural hydrogen isotopes are suitably analyzed without taking care of the contamination. Therefore, the hydrous wadsleyite crystal of sufficient size and homogeneity in the present study has been measured at TOPAZ instrument at SNS without any problem. Whereas full structure refinement of this wadsleyite crystal is currently in progress, it was preliminary shown that hydrogen occupancy in the M3 site is much closer to the value that estimated from C_{H2O} of the crystal (Purevjav et al. 2014b). We will report the refinement result elsewhere in near future.

Hydrous ringwoodite crystals

Single crystals of hydrous ringwoodite of up to 1000 μm were synthesized in the four relevant experimental runs (Table 1). Figure 2(c) shows one of the largest crystals from the EP13-3 run, which to the best of our knowledge is greater than any size reported in previous research. Such growth of ringwoodite requires a larger reduction in temperature (by 110 °C) compared with that in the case of wadsleyite. The other runs with smaller changes in temperature (HR14) or constant temperatures (HR12 and EP12-6) resulted in smaller sizes, between 200 μm and 600 μm. These ringwoodite crystals were grown between 1260 °C and 1400 °C, where they were observed to coexist with silicate melt, as expected from the relevant phase relations (Ohtani et al. 2000). For the EP13-3 run, we observed that about half of the sample volume was melted, whereas the other runs had smaller melt fractions. It was demonstrated from these observations that the growth rate changed largely with time. The rate was very rapid during initial crystallization and then became slower and slower during subsequent recrystallization with the melt-crystal interface kept close to the chemical equilibrium. The growth rate in the latter stage was moderately enhanced by precipitation of crystal volume upon reduction of the temperature, and an effective combination of these two processes made it possible to produce the single crystals of ringwoodite of 1 mm size in the EP13-3 run.

A precession photograph of the crystal shown in Figure 2(c) was captured along the [001] direction (Figure 3(c)). The photograph shows sharp diffraction spots, and no extra spot was observed. Moreover, SCXRD results of the two ringwoodite crystals taken from the HR12 and EP12-6 runs showed no intensity for the forbidden reflections, and no effect of twinning on their X-ray intensity data. The major element compositions in the cross sections of five crystals from the EP12-6 run and four crystals from the HR13-3 run showed little variations of Mg/Si = 1.92 ±0.01 and (Mg+Fe)/Si = 1.93 ± 0.02, respectively (Figure 4(a)). These results indicate that slow cooling of the crystals in large melt fraction is suitable for growing homogeneous ringwoodite crystals. Using the refined lattice constants of the ringwoodite crystals by PXRD and SCXRD, the C_{H2O} of each run product was estimated along the relation between unit cell volume V_0 and C_{H2O} (Ye et al. 2012). The estimated C_{H2O} were between 2.0 wt% and 2.6 wt% (Table 2), which were close to the uppermost values of previously observed C_{H2O} in hydrous ringwoodite (Inoue et al. 1998; Kudoh et al. 2000; Ye et al. 2012). It is suggested that the C_{H2O} in ringwoodite increases with increasing synthesis duration; the highest C_{H2O} of 2.6% among the current crystal products was synthesized after 12 h of heating, which is indeed the most lengthy among all synthesis experiments of the hydrous ringwoodite. The following SIMS results shows no evidence of zoning of C_{H2O}, so that the increase

463 of C_{H2O} with time is not because of diffusion of H_2O into the ringwoodite crystals after
464 their growth. Another possible process such as Mg^{2+}–Si^{4+} site disorder involving
465 hydrogen may be additionally considered (Kudoh et al. 2000).

466 Hydrogen isotope concentrations were analyzed by SIMS for the polished cross
467 sections of several ringwoodite crystals from the HR12 and EP12-6 runs. Although the
468 HR12 product crystals were synthesized from fully deuterated starting materials, it was
469 proved to have been extensively exchanged with hydrogen having natural isotope
470 abundance. The isotope abundance of hydrogen were uniformly distributed at D/(H +
471 D) = 45 ± 3% among all five crystals from the HR12 run (Figure 6). As in the case of
472 phase E synthesis, such incorporation of outside hydrogen most likely occurred through
473 its diffusion from outside of the capsule, which is inevitably more extensive for the
474 ringwoodite synthesized at a temperature 300 °C higher than that for the phase E. It is
475 therefore concluded that complete deuteration of ringwoodite crystals using the current
476 cell design and experimental condition is difficult. On the other hand, the EP12-6
477 product were synthesized from starting materials containing hydrogen with natural
478 isotope abundance. The five measured crystals consistently showed a very uniform
479 hydrogen concentration of 1.6 ± 0.1 wt% (Figure 6). By all these analytical results, it
480 was demonstrated that the slow-cooling method is suitable for growing

481 homogeneously-hydrous ringwoodite crystals which are appropriate for TOF single
482 crystal diffraction.

483

484 **Bridgmanite crystals**

485 Single crystals of bridgmanite with three different composition types were
486 synthesized in the five relevant experimental runs (Table 1). The largest were
487 iron-bearing bridgmanite crystals from the 5k2417 run at up to 600 μm in the largest
488 dimension (Figure 2(d)). These crystals were grown from the starting materials having
489 silicate compositions between $(Mg,Fe)_2SiO_4$ and $(Mg,Fe)SiO_3$, which are effective for
490 preventing stishovite crystal inclusions (Shatskiy et al., 2007). Moreover, existence of
491 H_2O significantly facilitates the crystal growth of bridgmanite (Ito and Weidner. 1986;
492 Shatskiy et al. 2007). The BSE image of these crystals showed their high homogeneity
493 (Figure 7), which is consistent with the major element compositions measured in the
494 cross sections of several different crystals from two experimental runs 5k2174 and
495 5k2179 (Figure 4(b)). These results indicated that the slow cooling in water-bearing
496 conditions is certainly effective for growing homogeneous bridgmanite crystals of
497 moderate sizes, while the cell design and the experimental conditions are still necessary
498 to be improved for growing the crystals 1 mm in size.

We confirmed the existence of hydrous silicate melt at temperature conditions of 1650 °C to 1760 °C, from which crystal growth occurred in the present study. This is consistent with the reported phase relations at hydrous condition (Ito and Weidner. 1986; Ohtani et al. 2000). We found that fine-tuning of the initial temperature and the extent of its decrease is not essential for increasing the crystal size, whereas a longer heating duration is definitely effective. From these observations it is inferred that recrystallization during the lengthy heating is more effective process for increasing crystal size of bridgmanite, compared with growth through crystal precipitation from the melt by reduction of temperature. In addition, it was demonstrated that sizes of aluminous bridgmanite crystals from the 5k2179 run were smaller than those of non-aluminous bridgmanite from the other runs. It was recently reported that such aluminous bridgmanite synthesized in hydrous conditions contains a significant amount of H_2O up to almost 1 wt% (Inoue et al. 2012), whereas non-aluminous bridgmanite grown in hydrous conditions contains only a few hundreds of ppm of H_2O (Litasov et al. 2003; Shatskiy et al. 2007). Apparently, a consideable amount of future study is required for growing highly hydrous, alumina-bearing bridgmanite crystals suitable for analysis of hydrogen by single crystal neutron diffraction.

516 The thermal gradient in the growth environment for the bridgmanite (Figure 1(b)) is
517 presumably comparable to or smaller than that for the phase E, wadsleyite or
518 ringwoodite (Figure 1(a)), because the capsule dimensions were smaller and the thermal
519 insulator was about 70% thicker. In addition, at the significantly higher temperature
520 conditions used for the bridgmanite synthesis, more efficient radiative heat transfer was
521 expected along the semi-transparent MgO sleeve body, which had an increased grain
522 size after the lengthy heating (Hofmeister 2005). Although we cannot evaluate the
523 actual gradient in a quantitative manner, the expectation was qualitatively consistent
524 with the observed crystal shape of bridgmanite. The shape was mostly euhedral
525 throughout the entire capsule volume of all five runs, rather than the fan-shaped,
526 needle-like aggregate type synthesized in the cells with thermal gradients significantly
527 larger than 20 °C/mm (Ito and Weidner 1986; Shatskiy et al. 2007).

528 We finally note that a part of the bridgmanite crystal products in the present study
529 has been successfully applied for in-situ radiative thermal conductivity measurements
530 via optical absorption spectroscopy in a high-pressure diamond anvil cell (Goncharov et
531 al. submitted). We are also planning to utilize these crystals for high-pressure studies of
532 electronic spin and valence states of iron in the lower-mantle bridgmanite using
533 synchrotron X-ray emission and Mössbauer spectroscopy, in addition to single-crystal

elasticity measurements of iron-bearing bridgmanite in the lower mantle using impulsive stimulated light scattering and Brillion light scattering.

Implications

It has been demonstrated that slow cooling in a Kawai-type cell is the best suitable method to synthesize homogeneous silicate crystals of 600 μm to 1100 μm sizes at pressures to 24 GPa. Degree of temperature reduction to facilitate the growth is necessary to be evaluated and optimized for each phase. Loeffert et al. (2002) used the slow-cooling method at 6 GPa in a belt press to grow a $SrCu_2O_3$ crystal 2 mm in size. The method in the present study should be applicable for the crystal growth of such an oxide phase at pressures at least up to 20 GPa; it may provide a new application of the Kawai cell in the field of material sciences by exploiting its high thermal stability and controllability at such pressure regime.

For applications of the product crystals in the present study, we emphasize that synthetic single crystals at very high pressures have now become measurable by neutron diffraction. The result is newly allowing us to determine a hydrogen site occupancy of the contamination-free crystal in terms of isotopes. Moreover, TOF single crystal diffraction instruments provide about twice or even higher spatial resolution than

553 previously used powder instruments; D20 at Institut Laue-Langevin was used at d_{min} =
554 0.96 Å for analyzing the deuterated wadsleyite powder (Sano-Furukawa et al. 2011),
555 whereas TOPAZ was used at d_{min} = 0.50 Å (Schultz et al. 2014) and SXD at ISIS was
556 used at d_{min} = 0.31 Å (Artioli et al. 1995) for analyzing single crystal samples. The
557 significantly smaller d_{min} by these TOF single crystal instruments is because it is the
558 best sensitive scheme for detecting diffraction at small *d*-values which is induced by
559 neutrons of short wavelengths. Thus, the geometry of chemical bonding around a
560 hydrogen atom in the deep-mantle hydrous minerals, including the distances of covalent
561 and hydrogen bonding and the angle between them, are determined with significantly
562 higher accuracy. Using these we will critically evaluate the proposed relations between
563 the bonding geometry and Raman and Infrared spectra of hydrogen which includes that
564 recently proposed by Panero et al. (2013) and their referred previous studies. Bonding
565 geometries predicted by previous theoretical calculations of deep-mantle hydrogen will
566 also be evaluated.

567 We finally note that all crystals in each sample capsule in the present study have a
568 uniform chemical composition. Therefore, lattice parameters, water concentration and
569 major element compositions of a candidate crystal can be promptly evaluated by PXRD
570 and EPMA results of the other crystals without destroying the candidate itself, which

make it easy and straightforward to select the best sample for single crystal diffraction. Such a pre-evaluation is essential to avoid wasting invaluable neutron beam time by measuring an inappropriate crystal.

Acknowledgments

This work was supported by JSPS grants-in-aid for Scientific Research (No. 23340161, 23540558, and 26287135). Visits to the Institute for Study of the Earth's Interior by J. F. Lin, L. Schoneveld, and H. Hwang were supported by a special grant from the Ministry of Education, Culture, Sports, Science and Technology. Part of the research conducted at J-PARC was through MLF user program (No. 2012B0016), where S. Harjo and J. Abe are acknowledged for technical supports. Part of the research conducted at SNS, Oak Ridge National Laboratory was sponsored by the Scientific User Facilities Division, Office of Basic Energy Sciences, US Department of Energy, where C. Hoffman and X. Wang are acknowledged for technical supports. T.O. acknowledges support from X-ray Free Electron Laser Priority Strategy Program (MEXT) for part of the research. J. F. Lin acknowledges support from the U.S. National Science Foundation Geophysics Program (NSF EAR Early Career), Energy Frontier Research in Extreme Environments (EFree), and Center for High Pressure Science and Advanced

590 Technology (HPSTAR) for part of the research. The authors thank Chikako Oka and
591 Eiji Ito for technical supports and discussion in conducting Kawai-type experiments,
592 Megan Matheney for manuscript editing, and Anton Shatskiy and one anonymous
593 reviewer for providing constructive comments to improve the manuscript.
594
595

References cited

Artioli, G., Rinaldi, R., Wilson, C.C., and Zanazzi, P.F. (1995) Single-crystal pulsed neutron diffraction of a highly hydrous beryl. Acta Cryst., B51, 733-737.

Bercovici, D., and Karato, S. (2003) Whole-mantle convection and the transition-zone water filter. Nature, 425, 39-44.

Bolfan-Casanova, N., Keppler, H., and Rubie, D.C. (2000) Water partitioning between nominally anhydrous minerals in the $MgO–SiO_2–H_2O$ system up to 24 GPa: implications for the distribution of water in the Earth's mantle. Earth and Planetary Science Letters, 182(3-4), 209-221.

Chakoumakos, B.C., Horita, J., and Garlea, V.O. (2013) H/D isotope effects in brucite at low temperatures. American Mineralogist, 98, 1-6.

Chen, J.H., Inoue, T., Weidner, D.J., Wu, Y.J., and Vaughan, M.T. (1998) Strength and water weakening of mantle minerals, olivine, wadsleyite and ringwoodite, Geophysical Research Letters, 25(4), 575-578.

Frost, D.J., Poe, B.T., Trønnes, R.G., Liebske, C., Duba, A., and Rubie, D.C. (2004) A new large-volume multianvil system. Physics of the Earth and Planetary Interiors, 143–144(0), 507-514.

Ghosh, S., Ohtani, E., Litasov, K.D., Suzuki, A., Dobson, D., and Funakoshi, K. (2013) Effect of water in depleted mantle on post-spinel transition and implication for 660 km seismic discontinuity. Earth and Planetary Science Letters, 371, 103-111.

Greenwood, J.P., Itoh, S., Sakamoto, N., Warren, P., Taylor, L., and Yurimoto, H. (2011) Hydrogen isotope ratios in lunar rocks indicate delivery of cometary water to the Moon. Nature Geoscience, 4, 79-82.

Harjo, S., Moriai, A., Torii, S., Suzuki, H., Suzuya, K., Morii, Y., Arai, M., Tomota, Y., Akita, K., and Akiniwa, Y. (2006) Design of engineering diffractometer at J-PARC. Materials Science Forum, 524-529, 199-204.

Hofmeister, A.M. (2005) Dependence of diffusive radiative transfer on grain-size, temperature, and Fe-content: Implications for mantle processes. Journal of Geodynamics, 40(1), 51-72.

Horita, J., dos Santos, A., Tulk, C., Chakoumakos, B., and Polyakov, V. (2010) High-pressure neutron diffraction study on H–D isotope effects in brucite. Physics and Chemistry of Minerals, 37(10), 741-749.

629 Huang, X., Xu, Y., and Karato, S.-i. (2005) Water content in the transition zone from
630 electrical conductivity of wadsleyite and ringwoodite. Nature, 434(7034),
631 746-749.
632 Inoue, T. (1994) Effect of water on melting phase relations and melt composition in
633 the system Mg_2SiO_4-$MgSiO_3$-H_2O up to 15 GPa. Physics of the Earth and
634 Planetary Interiors, 85, 237-263.
635 Inoue, T., Wada, T., Sasaki, R., and Yurimoto, H. (2010) Water partitioning in the
636 Earth's mantle. Physics of the Earth and Planetary Interiors, 183(1–2),
637 245-251.
638 Inoue, T., Weidner, D.J., Northrup, P.A., and Parise, J.B. (1998) Elastic properties of
639 hydrous ringwoodite (g-phase) in Mg_2SiO_4. Earth and Planetary Science
640 Letters, 160, 107-113.
641 Inoue, T., Yabuki, T., and Yurimoto, H. (2012) Water contents of Al-bearing
642 minerals in the mantle transition zone and the lower mantle. In T. Okuchi,
643 Ed. Joint Symposium of Misasa-2012 and Geofluid-2, p. P21-02. ISEI, Misasa,
644 Tottori, Japan.
645 Inoue, T., Yurimoto, H., and Kudoh, Y. (1995) Hydrous modified spinel,
646 $Mg_{1.75}SiH_{0.5}O_4$: a new water reservoir in the mantle transition region.
647 Geophysical Research Letters, 22, 117-120.
648 Ito, E., and Weidner, D. J. (1986) Crystal growitn of $MgSiO_3$ perovskite. Geophysical
649 Research Letters, 13(5), 464-466.
650 Jacobsen, S.D., Smyth, J.R., Spetzler, H., Holl, C.M., and Frost, D.J. (2004) Sound
651 velocities and elastic constants of iron-bearing hydrous ringwoodite.
652 Physics of the Earth and Planetary Interiors, 143–144(0), 47-56.
653 Jacobsen, S.D., Demouchy, S., Frost, D.J., Ballaran, T.B., and Kung, J. (2005) A
654 systematic study of OH in hydrous wadsleyite from polarized FTIR
655 spectroscopy and single-crystal X-ray diffraction: Oxygen sites for hydrogen
656 storage in Earth□s interior. American Mineralogist, 90, 61-70.
657 Jorgensen, M.R.V., Hathwar, V.R., Sist, M., Wang, X., Hoffmann, C.M., Briseno, A.L.,
658 Overgaard, J., and Iversen, B.B. (2014) Accurate atomic displacement
659 parameters from time-of-flight neutron-diffraction data at TOPAZ. Acta
660 Crystallographica, A70, 679-681.
661 Kanzaki, M. (1991) Stability of hydrous magnesium silicates in the mantle
662 transition zone. Physics of the Earth and Planetary Interiors, 66, 307-312.

Keppler, H., and Smyth, J.R. (2006) Water in Nominally Anhydrous Minerals. Reviews in Mineralogy and Geochemistry, 62, p. 478. Mineralogical Society of America, Washington D. C.

Kleppe, A.E., Jephcoat, A.P., and Ross, N.L. (2001) Raman spectroscopic studies of phase E to 19 GPa. American Mineralogist, 86, 1275-1281.

Kohlstedt, D.L., Keppler, H., and Rubie, D.C. (1996) Solubility of water in the alpha, beta and gamma phases of $(Mg,Fe)_2SiO_4$. Contributions to Mineralogy and Petrology, 123(4), 345-357.

Kubo, T., Ohtani, E., Kato, T., Shinmei, T., and Fujino, K. (1998) Effects of Water on the α-β Transformation Kinetics in San Carlos Olivine. Science, 281(5373), 85-87.

Kudoh, Y., Finger, L.W., Hazen, R.M., Prewitt, C.T., Kanzaki, M., and Veblen, D.R. (1993) Phase E: A high pressure hydrous silicate with unique crystal chemistry. Physics and Chemistry of Minerals, 19(6), 357-360.

Litasov, K., Ohtani, E., Langenhorst, F., Yurimoto, H., Kubo, T., and Kondo, T. (2003) Water solubility in Mg-perovskites, and water storage capacity in the lower mantle. Earth and Planetary Science Letters, 211(1-2), 189-203.

Litasov, K., Shatskiy, A., Ohtani, E., and Katsura, T. (2011) Systematic study of hydrogen incorporation into Fe-free wadsleyite. Physics and Chemistry of Minerals, 38(1), 75-84.

Loeffert, A., Gross, C., and Assmus, W. (2002) Crystal growth under high pressure: preparation of the spin-ladder compound $SrCu_2O_3$. Journal of Physics: Condensed Matter, 14(44), 11161.

Mao, Z., Jacobsen, S.D., Frost, D.J., McCammon, C.A., Hauri, E.H., and Duffy, T.S. (2011) Effect of hydration on the single-crystal elasticity of Fe-bearing wadsleyite to 12 GPa. American Mineralogist, 96(10), 1606-1612.

Mao, Z., Lin, J.-F., Jacobsen, S.D., Duffy, T.S., Chang, Y.-Y., Smyth, J.R., Frost, D.J., Hauri, E.H., and B., P.V. (2012) Sound velocities of hydrous ringwoodite to 16 GPa and 673 K. Earth and Planetary Science Letters, 331-332, 112-119.

McCammon, C.A., Frost, D.J., Smyth, J.R., Laustsen, H.M.S., Kawamoto, T., Ross, N.L., and van Aken, P.A. (2004) Oxidation state of iron in hydrous mantle phases: implications for subduction and mantle oxygen fugacity. Physics of the Earth and Planetary Interiors, 143, 157-169.

Miyagi, I., and Yurimoto, H. (1995) Water content of melt inclusions in phenocrysts using secondary ion mass spectrometer. Bulletin of the Volcanological Society of Japan, 40, 349-355.

699 Mrosko, M., Lenz, S., McCammon, C.A., Taran, M., Wirth, R., and Koch-Muller, M.
700 (2013) Hydrogen incorporation and the oxidation state of iron in
701 ringwoodite: A spectroscopic study. American Mineralogist, 98(4), 629-636.
702 Ohtani, E., Litasov, K., Hosoya, T., Kubo, T., and Kondo, T. (2004) Water transport
703 into the deep mantle and formation of a hydrous transition zone. Physics of
704 The Earth and Planetary Interiors, 143–144(0), 255-269.
705 Ohtani, E., Mizobata, H., and Yurimoto, H. (2000) Stability of dense hydrous
706 magnesium silicate phases in the systems Mg_2SiO_4-H_2O and $MgSiO_3$-H_2O at
707 pressures up to 27 GPa. Physics and Chemistry of Minerals, 27(8), 533-544.
708 Okuchi, T. (1997) Hydrogen partitioning into molten iron at high pressure:
709 Implications for Earth's core. Science, 278, 1781-1784.
710 Okuchi, T., Tomioka, N., Purevjav, N., Abe, J., Harujo, S., and Gong, W. (2014)
711 Structure refinement of sub-cubic-mm volume sample at high pressures by
712 pulsed neutron powder diffraction: application to brucite in an opposed
713 anvil cell. High Pressure Research, 34, 273-280.
714 Panero, W.R., Smyth, J.R., Pigott, J.S., Liu, Z.X., and Frost, D.J. (2013) Hydrous
715 ringwoodite to 5 K and 35 GPa: Multiple hydrogen bonding sites resolved
716 with FTIR spectroscopy. American Mineralogist, 98(4), 637-642.
717 Pearson, D.G., Brenker, F.E., Nestola, F., McNeill, J., Nasdala, L., Hutchison, M.T.,
718 Matveev, S., Mather, K., Silversmit, G., Schmitz, S., Vekemans, B., and Vincze,
719 L. (2014) Hydrous mantle transition zone indicated by ringwoodite
720 included within diamond. Nature, 507(7491), 221-224.
721 Purevjav, N., Okuchi, T., Tomio ka, N., Abe, J. and Harujo, S. (2014a) Hydrogen site
722 analysis of hydrous ringwoodite in mantle transition zone by pulsed
723 neutron diffraction, Geophysical Research Letters, 41, 6718-6724.
724 Purevjav, N., Okuchi, T., Tomioka, N., Hoffmann, C. and X, Wang. (2014b) Unique
725 substitution mechanism of hydrogen in deep mantle wadsleyite
726 demonstrated by time of flight single-crystal Laue diffraction, Japanese
727 Society of Neutron Science 2014 Annual Meeting Abstract Volume, Sapporo,
728 Japan.
729 Rudolph, P. (2010) Defect Formation During Crystal Growth from the Melt. In G.
730 Dhanaraj, K. Byrappa, V. Prasad, and M. Dudley, Eds. Springer Handbook of
731 Crystal Growth, p. 159-201. Springer Berlin Heidelberg.
732 Sano-Furukawa, A., Kuribayashi, T., Komatsu, K., Yagi, T., and Ohtani, E. (2011)
733 Investigation of hydrogen sites of wadsleyite: A neutron diffraction study.
734 Physics of The Earth and Planetary Interiors, 189(1–2), 56-62.

735 Schmandt, B., Jacobsen, S.D., Becker, T.W., Liu, Z.X., and Dueker, K.G. (2014)
736 Dehydration melting at the top of the lower mantle. Science, 344(6189),
737 1265-1268.
738 Schultz, A.J., Jorgensen, M.R.V., Wang, X., Mikkelson, R.L., Mikkelson, D.J., Lynch,
739 V.E., Peterson, P.F., Green, M.L., and Hoffmann, C.M. (2014) Integration of
740 neutron time-of-flight single-crystal Bragg peaks in reciprocal space.
741 Journal of Applied Crystallography, 47(3), 915-921.
742 Shatskiy, A., Fukui, H., Matsuzaki, T., Shinoda, K., Yoneda, A., Yamazaki, D., Ito, E.,
743 and Katsura, T. (2007) Growth of large (1 mm) $MgSiO_3$ perovskite single
744 crystals: A thermal gradient method at ultrahigh pressure. American
745 Mineralogist, 92(10), 1744-1749.
746 Shatskiy, A., Yamazaki, D., Borzdov, Y.M., Matsuzaki, T., Litasov, K., Cooray, T., Ferot,
747 A., Ito, E., and Katsura, T. (2010) Stishovite single-crystal growth and
748 application to silicon self-diffusion measurements. American Mineralogist,
749 95, 135-143.
750 Shatskiy, A., Katsura, T., Litasov, K.D., Shcherbakova, A.V., Borzdov, Y.M., Yamazaki,
751 D., Yoneda, A., Ohtani, E., and Ito, E. (2011) High pressure generation using
752 scaled-up Kawai-cell. Physics of the Earth and Planetary Interiors, 189,
753 92-108.
754 Shatskiy, A., Litasov, K.D., Matsuzaki, T., Shinoda, K., Yamazaki, D., Yoneda, A., Ito, E.,
755 and Katsura, T. (2009) Single crystal growth of wadsleyite. American
756 Mineralogist, 94(8-9), 1130-1136.
757 Shibazaki, Y., Ohtani, E., Terasaki, H., Suzuki, A., and Funakoshi, K. (2009) Hydrogen
758 partitioning between iron and ringwoodite: Implications for water
759 transport into the Martian core. Earth and Planetary Science Letters,
760 287(3-4), 463-470.
761 Shieh, S.R., Mao, H.K., Konzett, J., and Hemley, R.J. (2000) In-situ high pressure
762 X-ray diffraction of phase E to 15 GPa. American Mineralogist, 85, 765-769.
763 Smyth, J.R., Bolfan-Casanova, N., Avignant, D., El-Ghozzi, M., and Hirner, S.M. (2014)
764 Tetrahedral ferric iron in oxidized hydrous wadsleyite. American
765 Mineralogist, 99(2-3), 458-466.
766 Smyth, J.R., Holl, C.M., Frost, D.J., Jacobsen, S.D., Langenhorst, F., and McCammon,
767 C.A. (2003) Structural systematics of hydrous ringwoodite and water in
768 Earth's interior. American Mineralogist, 88(10), 1402-1407.

769 Tamura, S., Kato, K., and Goto, M. (1974) Single crystals of T-Nb2O5 obtained by
770 slow cooling method under high pressures. Zeitschrift für anorganische und
771 allgemeine Chemie, 410(3), 313-315.
772 Tomioka, N., Okuch, T., and Purevjav, N. (2014) Pulsed neutron diffraction study of
773 dense hydrous magnesium silicate phase E, DE5-A, International
774 Mineralogical Association 2014, Gauteng, South Africa, 2014.
775 Wenk, H.-R. (2006) Neutron Scattering in Earth Sciences. Reviews in Mineralogy
776 and Geochemistry, 63, p. 471. Mineralogical Society of America, Washington
777 D. C.
778 Yang, X.Z., Keppler, H., Dubrovinsky, L., and Kurnosov, A. (2014) In-situ infrared
779 spectra of hydroxyl in wadsleyite and ringwoodite at high pressure and
780 high temperature. American Mineralogist, 99(4), 724-729.
781 Ye, Y., Brown, D.A., Smyth, J.R., Panero, W.R., Jacobsen, S.D., Chang, Y.Y., Townsend,
782 J.P., Thomas, S.M., Hauri, E.H., Dera, P., and Frost, D.J. (2012) Compressibility
783 and thermal expansion of hydrous ringwoodite with 2.5(3) wt% H_2O.
784 American Mineralogist, 97(4), 573-582.
785 Yoshino, T., Manthilake, G., Matsuzaki, T., and Katsura, T. (2008) Dry mantle
786 transition zone inferred from the conductivity of wadsleyite and
787 ringwoodite. Nature, 451(7176), 326-329.
788 Yurimoto, H., Kurosawa, H., and Sueno, S. (1989) Hydrogen analysis in quartz
789 crystals and quartz glasses by secondary ion mass spectrometry.
790 Geochimica Et Cosmochimica Acta, 53, 751-755.
791

792 **Figure Captions**
793

794 **Figure 1.** Cell assembly designs for pressure generation (a) to 21 GPa coupled with 8
795 mm truncation edge length (TEL) and (b) to 24 GPa coupled with 6 mm TEL. Sintered
796 $MgO–Cr_2O_3$ pressure medium with octahedral edge length (OEL) = 14 mm were
797 commonly used for these cells. Dimensions of the sample capsules are shown at the
798 central areas of the cells.
799

800 **Figure 2.** Photographs of representative crystals synthesized in and recovered from the
801 high-pressure cells. Length of the scale bars is 500 μm unless explicitly shown. (a)
802 Phase E from PE02; (b) hydrous magnesian wadsleyite from HR18; (c) hydrous
803 magnesian ringwoodite from EP13-3; (d) iron-bearing bridgmanite from 5k2417.
804

805 **Figure 3.** Precession X-ray diffraction photographs of the single crystals. (a) Phase E
806 from PE02 along the [001] zone axis. (b) Hydrous wadsleyite from EP13-2 along the
807 [010] zone axis. The weak extra spots come from small wadsleyite crystals associated
808 with the host crystal. (c) Hydrous ringwoodite from EP13-3 along the [001] zone axis.
809 Numbers denote Miller indices of diffraction spots indicated by arrows. All of the
810 patterns show sharp diffraction spots from non-disordered single crystals.

811

812 **Figure 4.** Major-element compositions of recovered single crystals taken by electron
813 probe microanalyser (EPMA). (a) Results from Phase E (PE02), hydrous wadsleyite
814 (EP13-2), and hydrous ringwoodite (EP12-6 and EP13-3) run charges plotted in ternary
815 MgO–FeO–SiO_2 diagrams in molar ratio. (b) Results from MgFe-bearing bridgmanite
816 (5k2174) and MgFeAl-bearing bridgmanite (5k2179) run charges plotted in ternary
817 MgO–FeO–(Al_2O_3+SiO_2) and (MgO+FeO)–Al_2O_3–SiO_2 diagrams in molar ratio. These
818 data plots are surrounded by the squares with blue, purple or red color, which indicates
819 that they are close-up views of the areas indicated by the corresponding colors in the
820 entire triangle plots shown together. Each different color and symbol within these
821 close-up views shows the EPMA results taken from each different crystal in the same
822 run charge. The averaged chemical formula of MgFe- and MgFeAl-bearing bridgmanite
823 crystals (5k2174 and 5k2179, excluding their H_2O components which were not
824 analyzed) are $Mg_{0.96}Fe_{0.07}Si_{0.98}O_3$ and $Mg_{0.90}Fe_{0.13}Al_{0.11}Si_{0.90}O_3$, respectively.

825

826 **Figure 5.** Relative neutron diffraction linewidth profiles $\Delta d/d$ of phase E as a function
827 of d-spacing. Δd was defined as the full width at half maximum (FWHM) of each
828 reflection. Thin straight lines show expected $\Delta d/d$ positions when the described

829 temperature inhomogeneity exists within the entire capsule ($\Delta Temp$). Resolution of the
830 diffractometer optics is shown by the bold line ($\Delta Temp$ = 0 °C). Filled and open circles
831 denote the results obtained for the entire PE01 and PE02 run charges, respectively. A
832 Lorentz-type function was assumed for the lineshape of the observed reflections, where
833 the linewidth was approximated by the sum of that from the diffractiometer optics and
834 that from $\Delta Temp$.
835
836 **Figure 6.** Secondary ion mass spectroscopy (SIMS) results of hydrogen and deuterium
837 concentration distributions measured on polished cross sections of representative five
838 crystals selected from each of the three representative run charges (15 crystals in total).
839 (a, b) H_2O and D_2O concentrations of the deuterated phase E crystals recovered from
840 the PE02 run, respectively. (c, d) H_2O and D_2O concentrations of the deuterated
841 hydrous ringwoodite crystals recovered from the HR12 run, respectively. (e) H_2O
842 concentration of hydrous ringwoodite crystals recovered from the EP12-6 run. The
843 vertical scale shows recalculated H_2O or D_2O concentrations from their $H/^{30}Si$ or $D/^{30}Si$
844 ratios, respectively. In order to find compositional zoning or another heterogeneity
845 within each crystal, the distances between each measurement position and the nearest
846 rim of each cross section are shown in the horizontal scales. The broken lines show the

847 distances from the center of each cross section to its nearest rim; note that actual
848 dimension(s) of the measured crystals is larger than twice of these distances, because
849 these are the observed minimum only within each cross section. The standard deviation
850 of each water concentration value is estimated to be about 6 % of the value (indicated
851 by the error bars), which corresponds to the standard deviation of the measurement
852 results of the hornblende H_2O standard (15 points in total). D_2O within the PE02 and the
853 HR12 crystal products were partly exchanged for H_2O during the crystal growth.
854
855 **Figure 7.** Back-scattering electron (BSE) image of polished cross section of an
856 iron-bearing bridgmanite crystal from 5k2417. The scale bar is 100 μm in length.
857

Table 1. Experimental conditions and the maximum size of the recovered crystals

Run No.	Target phase	OEL/TEL [mm]	Load [MN]	Pressure [GPa]	Temperature [°C]	Duration [hours]	Starting materials	Size [μm]	Silicate melting
PE01	phase E	14/8	6.5	14	1100 / 1090	2	Mg_2SiO_4 +22 wt.% D_2O	500	No
PE02	phase E	14/8	6.5	14	1100 / 1100	3	Mg_2SiO_4 +22 wt.% D_2O	600	No
EP13-2	Mg wadsleyite	14/8	8.5	17	1300 / 1250	13	Mg_2SiO_4 + 10 wt.% H_2O	600	Yes
EP13-1	Mg wadsleyite	14/8	8.5	17	1400 / 1300	6	Mg_2SiO_4 + 10 wt.% H_2O	600	Yes
HW7	Mg wadsleyite	14/8	8.5	17	1400 / 1310	24	Mg_2SiO_4 + 10 wt.% H_2O	400	Yes
HW8	Mg wadsleyite	14/8	8.5	17	1400 / 1360	6	Mg_2SiO_4 + 15 wt.% H_2O	800	Yes
HW18	Mg wadsleyite	14/8	8.5	17	1390 / 1320	10	Mg_2SiO_4 + 15 wt.% H_2O	1100	Yes
HR14	Mg ringwoodite	14/8	19	21	1340 / 1310	1.5	Mg_2SiO_4 + 5 wt.% D_2O	200	Yes
HR12	Mg ringwoodite	14/8	19	21	1360 / 1360	2.5	Mg_2SiO_4 + 11 wt.% D_2O	600	Yes
EP13-3	Mg ringwoodite	14/8	19	21	1400 / 1290	12	Mg_2SiO_4 + 10 wt.% H_2O	1000	Yes
EP12-6	MgFe ringwoodite	14/8	9.6	18	1270 / 1260	1	$(Mg_{0.91}Fe_{0.09})_2SiO_4$ + 10 wt.% H_2O	300	Yes
5k2247	Mg bridgmanite	14/6	19	24	1710 / 1650	3	$Mg_{1.4}SiO_{3.4}$ + 9 wt.% H_2O	200	Yes
5k2221	Mg bridgmanite	14/6	19	24	1700 / 1700	8	$Mg_{1.3}SiO_{3.3}$ + 7 wt.% H_2O	300	Yes
5k2174	MgFe bridgmanite	14/6	19	24	1650 / 1650	5.5	$(Mg_{0.92}Fe_{0.08})_{1.5}SiO_{3.5}$ + 6 wt.% H_2O	100	Yes
5k2417	MgFe bridgmanite	14/6	19	24	1700 / 1670	12	$(Mg_{0.84}Fe_{0.16})_{1.8}SiO_{3.8}$ + 7 wt.% H_2O	600	Yes
5k2179	MgFeAl bridgmanite	14/6	19	24	1760 / 1750	7	$(Mg_{0.92}Fe_{0.08})_{1.5}SiO_{35}$ + $0.2Al_2O_3$ + 5 wt.% H_2O	100	Yes

858

Table 2. Crystallographic parameters of the recovered crystals

Run No.	Phase	Space group	Lattice constants [Å]			Unit cell vol.	Hydrogen
			a	*b*	*c*	V_0 [Å^3]	concentration [wt.%]
PE01	phase E	*R*-3m	2.9731(1)		13.913(1)	106.50(1)	N. A.
PE02	phase E	*R*-3m	2.9679(1)		13.888(1)	105.94(1)	1.0(1) (SIMS, H_2O) 6.9(5) (SIMS, D_2O)
EP13-2	Mg wadsleyite	*Imma*	5.6844(8)	11.527(2)	8.2532(7)	540.80(8)	1.6 (from *b*/*a*)
EP13-1	Mg wadsleyite	*Imma*	5.6852(4)	11.508(1)	8.2523(8)	539.92(10)	1.3 (from *b*/*a*)
HW7	Mg wadsleyite	*Imma*	5.6871(7)	11.512(2)	8.2568(8)	540.61(8)	1.3 (from *b*/*a*)
HW8	Mg wadsleyite	*Imma*	5.6879(6)	11.513(1)	8.2542(7)	540.55(8)	1.3 (from *b*/*a*)
HW18	Mg wadsleyite	*Imma*	5.6882(6)	11.497(1)	8.2554(8)	539.89(8)	1.1 (from *b*/*a*)
HR14	Mg ringwoodite	*Fd*-3*m*		8.0795(4)		527.41(8)	2.2(2) (from V_0)
HR12	Mg ringwoodite	*Fd*-3*m*		8.0773(3) 8.0771(5)*		526.99(6)	2.1(2) (from V_0) 0.6(1) (SIMS, H_2O) 0.5(0) (SIMS, D_2O)
EP13-3	Mg ringwoodite	*Fd*-3*m*		8.0834(2)		528.19(4)	2.6(2) (from V_0)
EP12-6	$Mg_{92}Fe_{08}$ ringwoodite	*Fd*-3*m*		8.0903(6)*		529.53(7)	2.0(2) (from V_0) 1.6(1) (SIMS, H_2O)

*determined by SCXRD

859

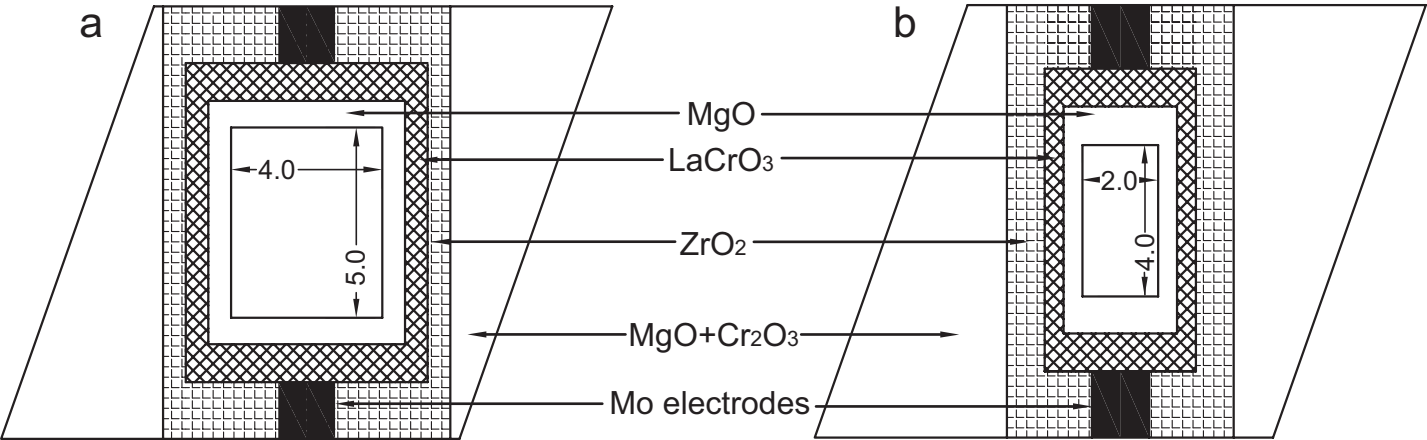
a
b
MgO
LaCrO3
ZrO2
MgO+Cr2O3
Mo electrodes
4.0
5.0
2.0
4.0

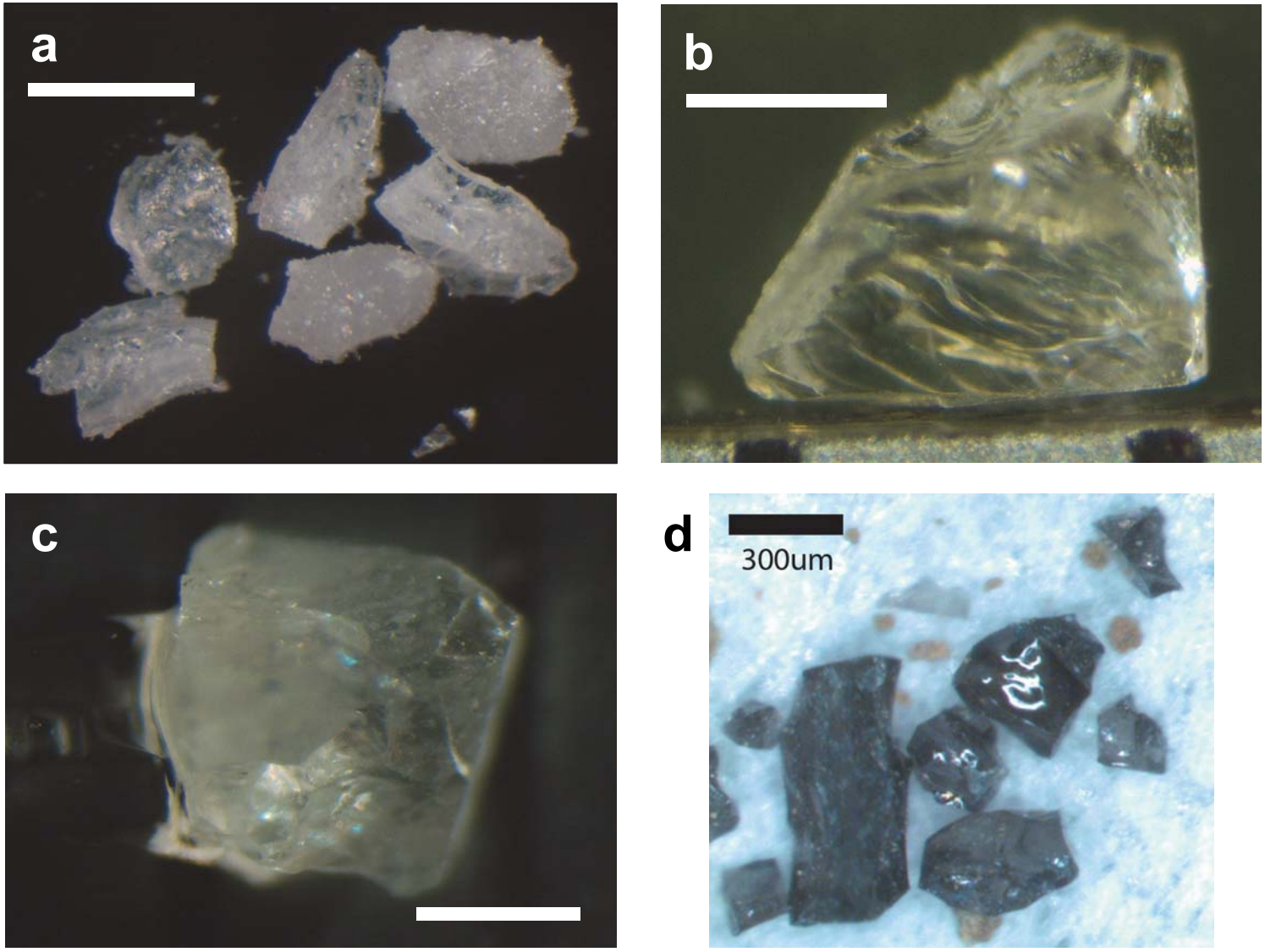
a
b
c
d
300um

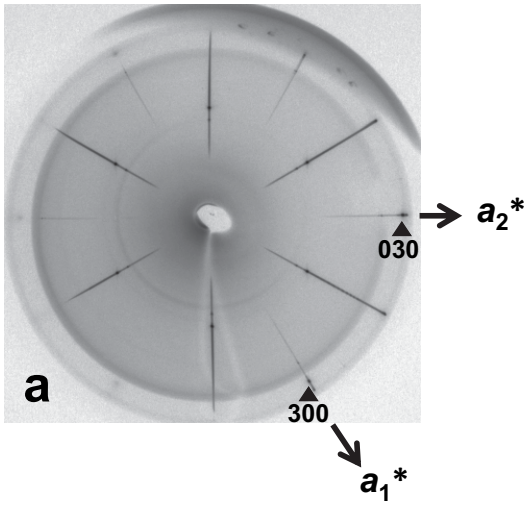
a
030
a_2*
300
a_1*

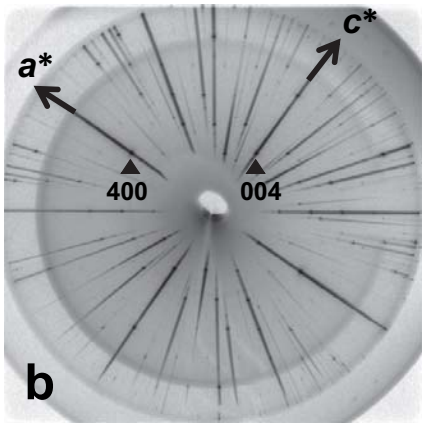
b
a*
c*
400
004

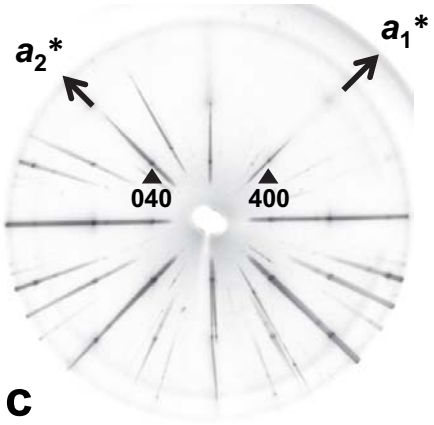
c
a_2*
a_1*
040
400

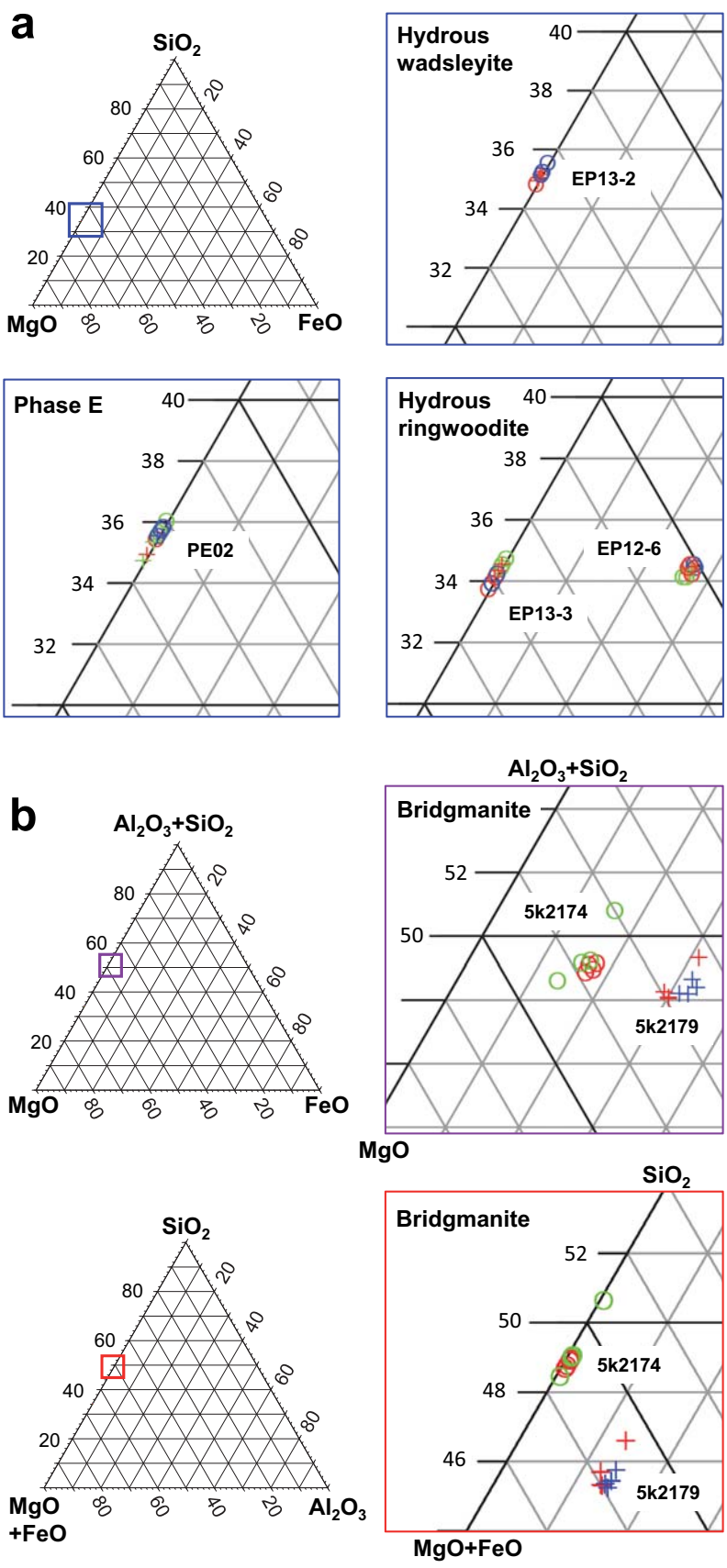
a
SiO2
MgO
FeO
Hydrous wadsleyite
EP13-2
Phase E
PE02
Hydrous ringwoodite
EP12-6
EP13-3
b
Al2O3+SiO2
MgO
FeO
Bridgmanite
5k2174
5k2179
SiO2
MgO +FeO
Al2O3
MgO+FeO

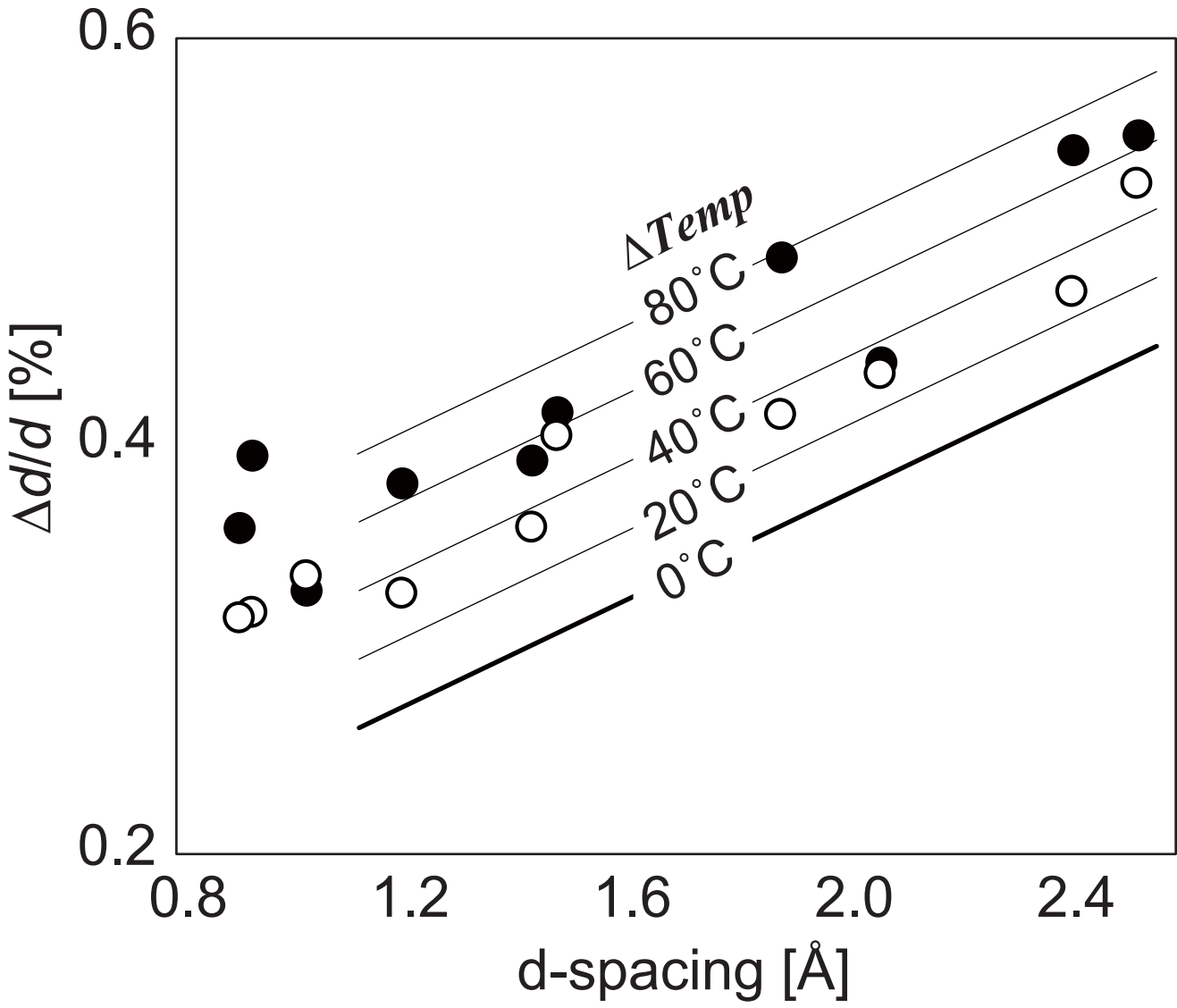
0.6
0.4
0.2
Δd/d [%]
0.8
1.2
1.6
2.0
2.4
d-spacing [Å]
ΔTemp
80˚C
60˚C
40˚C
20˚C
0˚C

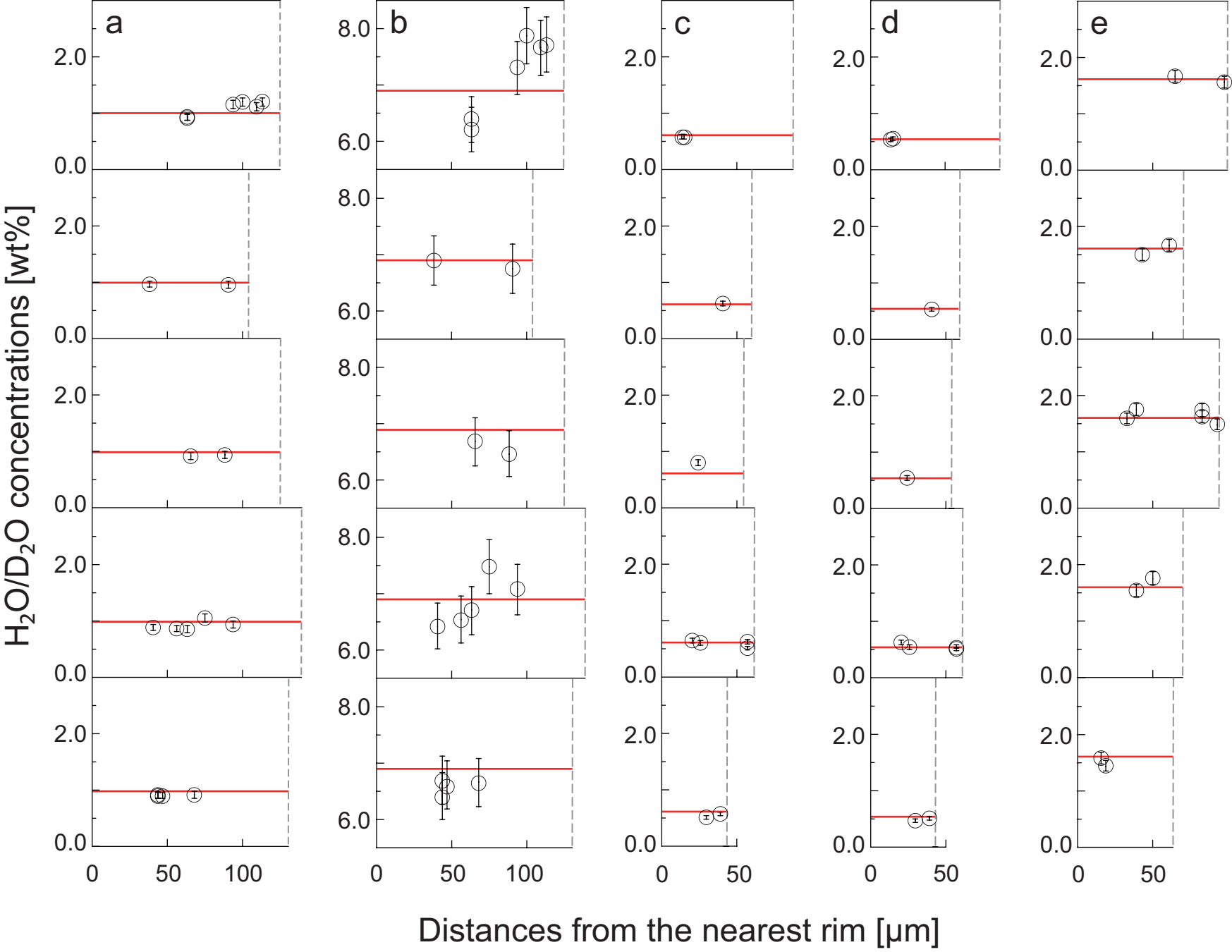
a
b
c
d
e
H_2O/D_2O concentrations [wt%]
Distances from the nearest rim [μm]